A macro-element for the modelling of shallow foundation deformations under seismic load

M.D.L. Millen[a,*], M. Cubrinovski[a], S. Pampanin[a,b], A. Carr[a]

[a] University of Canterbury, Private Bag 4800, Christchurch 8140, New Zealand
[b] University of Rome "La Sapienza", Via Eudossiana 18, Rome 00184, Italy

ABSTRACT

This paper presents a new soil-foundation macro-element model to allow efficient and sufficiently accurate consideration of soil-foundation-structure interaction in structural analysis. The model makes use of two constitutive models, a plasticity model which models the soil inelastic deformation, and an elastic uplift model, which captures the geometric non-linearity during uplift of the foundation. Further considerations are made to allow the macro-element to be efficiently implemented in a particular non-linear finite element software (Ruaumoko3D). Two experimental centrifuge tests are simulated using the proposed macro-element: one of a bridge pier and one of a one-bay, one-storey frame structure. The simulated results are compared to the experimental behaviour to demonstrate the accuracy of the numerical model.

1. Introduction

The consideration of soil deformations and soil-foundation-structure interaction (SFSI) in building design and analysis is becoming common place for structural engineers. This is largely motivated by a performance-based design philosophy where there is a need to understand and quantify the transient and residual deformations of the foundation and their influence on the overall behaviour of the soil-foundation-structure system.

The practicing engineering community is often constrained to considering the soil-foundation interface through a series of linear uncoupled springs and dashpots, which can miss some of the most beneficial effects of SFSI [32] as well as the potentially detrimental consequences [26]. An alternative approach is direct mesh finite-element modelling of the soil and structure can capture the non-linear effects, it requires a detailed understanding of soil and structural mechanics and behaviour of soil-foundation-structure systems under earthquake loading, as well as experience in finite element modelling. The need for a simple, reliable and sufficiently accurate numerical tool to predict the non-linear soil-foundation interface has prompted considerable development in lumped parameter approaches to consider soil-foundation-structure-interaction. SFSI is a branch of the widely discussed soil-structure interaction (SSI), which covers the behaviour of many different structures (e.g. pipelines, embankments, buildings). Many of the phenomenon and numerical issues that exist for SFSI are also apparent for many other SSI problems, however, SFSI deals directly with

foundation uplift and nonlinear soil behaviour, whereas typical SSI analyses make use of equivalent linear properties and such non-linearities are beyond their scope.

Two different numerical approaches dominate this type of analysis, the conventional Winkler-beam and the macro-element approach. The Winkler-beam uses a series of independent translational springs that can yield and detach (eg. [13,21]) The combination of the springs provides the rotational and vertical stiffness of the footing, while an additional uncoupled translational spring models horizontal stiffness. On the other hand, the macro-element models the rotational, horizontal and vertical stiffness of the foundation directly using coupled translational and rotational springs. The condensation down to only one spring for each degree-of-freedom or mode of deformation (axial, shear and moment) is possible by assuming that the footing itself acts as a rigid body. The non-linear effects, such as uplifting and soil yielding, are captured by considering the coupling of the forces through a coupled hysteretic model. Dashpot elements can be added in parallel to the macro-element to model the radiation damping in each degree-of-freedom.

One of the difficulties with the Winkler-beam approach is that the rotational and vertical stiffnesses are determined from the same springs, which limits its ability to accurately model behaviour in the non-linear range. The macro-element is less limited since it uses separate springs that are coupled through constitutive equations to capture non-linear behaviour and for this reason the authors have chosen to continue to develop and validate it within this paper.

Nomenclature

h	Magnitude of plastic modulus
h_0	Plastic modulus parameter
K	Stiffness matrix
L	Length of foundation in the plane of loading
M	Applied foundation moment
N	Applied foundation axial load
N_{max}	Ultimate bearing capacity of the foundation
p_1	Ratio of axial stiffness used in the plasticity modulus
p_2	Parameter to control stiffness of reload behaviour
Q	Normalised foundation loads
$Q_{M,max}$	Normalised ultimate capacity of foundation under eccentric load
$Q_{V,max}$	Normalised pseudo shear capacity of soil-foundation interface
$q_{m,uplift}$	Pseudo uplift angle
q	Normalised foundation displacement
V	Applied foundation shear load
α	Uplift parameter
χ	Plasticity surface normalised shear parameter
δ	Uplift parameter
δ_N	Vertical foundation displacement
δ_V	Horizontal foundation displacement
ϵ	Uplift parameter
γ	Uplift parameter
κ	Normalised stiffness
Λ	Normalised distance to bounding surface
λ	Plasticity surface normalised moment parameter
θ	Foundation rotation
ξ	Bounding surface parameter to control the normalised axial load
ζ	Uplift-plasticity coupling parameter

The first macro-element for modelling soil behaviour was suggested as early as Roscoe and Schofield [34], while the full development of a plasticity framework for monotonic loading was achieved by Nova and Montrasio [29] with a non-associative flow rule for a foundation on sand. Additional developments of this model include (eg. [22,12,2]). Paolucci [30] was the first to implement a macro-element into dynamic seismic analysis using an elastic-perfectly plastic formulation. Cremer et al. [8,9] included a distinct uplift mechanism which was combined with the plasticity model to give the overall response for strip footings on cohesive soils. The Paolucci et al. [31] model introduced a degradation factor to account for softening of the response due to the rounding of the soil contact surface from irrecoverable deformations. Chatzigogos et al. [6] developed a model with coupled plasticity and uplift mechanisms for undrained soil conditions. Chatzigogos et al. [5] extended the Chatzigogos et al. [6] model to capture frictional soils and frictional sliding with a non-associative flow rule. Figini et al. [15] used the bounding surface suggested by the failure envelope from Nova and Montrasio [29] to model foundations on sand and used a vertical mapping rule to define the image point resulting in improved simulation of settlement under small cycles. Figini et al. [15] adopted the degradation model used by Paolucci et al. [31] and the uplift formulation was based on works by Wolf [39]. The experimentally validated macro-element model developed by Figini et al. [15] gives good approximations to base moment, base shear, rotation, translation and settlement, with validations against experimental single and multiple degree-of-freedom experimental shake table tests from Negro et al. [28], Combescure and Chaudat [7] and Shirato et al. [36].

The macro-element formulation presented in this paper uses the uplift model from Chatzigogos et al. [6], and the plasticity formulation from Figini et al. [15]. Additional modifications have been made to allow the model to be implemented into the time history based structural analysis software, Ruaumoko3D [4]. The formal validation of the new macro-element formulation was performed as part of a larger study into the performance-based design of building-foundation systems [24,25].

2. Characteristics of the macro-element

Most structural time-history analysis software solves the equations of motion in the force, displacement and time domain, while to provide a generalised macro-element model the displacements and forces in the macro-element formulation must be normalised using Eqs. (1)–(3).

The forces (N - axial load, V - shear load, M - moment load), displacements (δ_N - axial displacement, δ_V - shear displacement, θ_M - rotation) and stiffnesses (K_{glob}) have been normalised by the static ultimate axial capacity of the footing (N_{max}) and the footing length (L)

respectively. The use of Q for normalised forces and lowercase q for normalised forces is consistent with previous formulations of macro-elements (eg. [15]).

$$Q = [Q_N, Q_V, Q_M] = \left[\frac{N}{N_{max}}, \frac{V}{N_{max}}, \frac{M}{N_{max}L}\right] \tag{1}$$

$$q = [q_N, q_V, q_M] = \left[\frac{\delta_N}{L}, \frac{\delta_V}{L}, \theta_M\right] \tag{2}$$

$$\kappa = \begin{bmatrix} \kappa_{NN} & \kappa_{VN} & \kappa_{MN} \\ \kappa_{NV} & \kappa_{VV} & \kappa_{MV} \\ \kappa_{NM} & \kappa_{VM} & \kappa_{MM} \end{bmatrix} = \frac{K_{glob}}{N_{max}} \begin{bmatrix} L & L & 1 \\ L & L & 1 \\ 1 & 1 & 1/L \end{bmatrix} \tag{3}$$

The stiffness matrix (κ) is composed of two components connected in series, the 'elastic' stiffness and the plastic stiffness, which result in elastic and plastic displacements (Eqs. (4) and (5)). The elastic stiffness accounts for the elastic impedance of the soil based on the foundation geometry and soil stiffness, as well as effects of the geometric non-linearity associated with uplift behaviour. The 'plastic' stiffness captures the plastic deformation associated with the yielding of the soil.

$$\frac{1}{\kappa} = \frac{1}{\kappa^{elastic}} + \frac{1}{\kappa^{plastic}} \tag{4}$$

$$q = q^{elastic} + q^{plastic} \tag{5}$$

2.1. Linear-elastic stiffness

For the purely linear-elastic case with minimal embedment, the off diagonal stiffness terms are negligible, therefore the elastic stiffness matrix consists of only the following impedance terms.

$$\kappa_{elastic} = \begin{bmatrix} \kappa_{NN} & 0 & 0 \\ 0 & \kappa_{VV} & 0 \\ 0 & 0 & \kappa_{MM} \end{bmatrix} \tag{6}$$

The diagonal terms can be approximated based on the foundation impedances and fitted over a frequency range of interest (eg. [27]).

2.2. Uplift formulation

Uplift of a footing results in a reduction in the elastic stiffness due to a reduction in the soil-footing contact area.

As the footing rotates the displacements must be represented by the macro-element at a single point (Fig. 1). The formulation implemented in Figini et al. [15], which captures the displacements at the centre of the compliant part of the footing is not compatible for complex structures modelled using finite element software where the geometry must
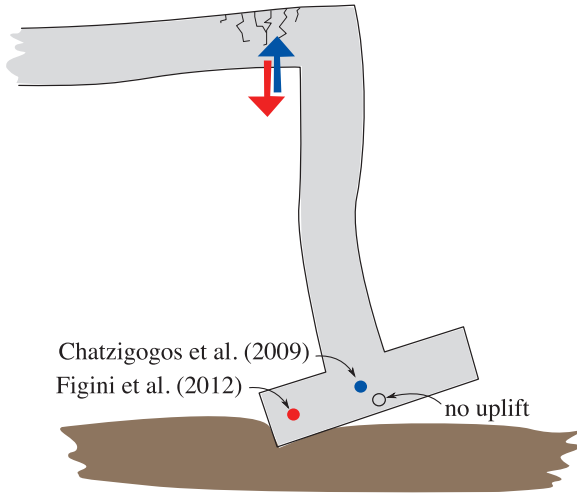
Fig. 1. Different global behaviour from different uplift formulations.

be directly represented through nodes and elements. The uplift formulation from Chatzigogos et al. [6] was chosen as it captures the displacements at the centre of the footing, a common location for joining columns, which allows the correct global behaviour to be passed to other elements in the structure.

The uplift formulation is based on a tangent stiffness matrix by first assuming that the horizontal (shear) stiffness (κ_{VV}) remains unaffected during uplift and the shear coupling terms are all equal to zero ($\kappa_{NV} = \kappa_{VN} = \kappa_{MV} = \kappa_{VM} = 0$). Uplift initiation is determined based on the moment exceeding some threshold level ($Q_{M,0}$) (Eq. (7)). The uplift limit in the formulation is given as a pseudo uplift angle ($q^{el}_{m,uplift}$) (Eq. (8)), where the normalised uplift moment is divided by the normalised elastic stiffness (κ_{MM}), and uplift occurs when the elastic component of rotation exceeds the pseudo uplift angle. For a purely elastic case, the rotation at which uplift would occur is equal to the pseudo uplift rotation, however, when soil plasticity is considered the actual rotation would be greater due to the reduction in rotational stiffness or addition of a plastic rotation component.

$$Q_{M,0} = \pm \frac{Q_N}{\alpha} \qquad (7)$$

$$q^{el}_{m,uplift} = \frac{Q_{M,0}}{\kappa_{MM}} \qquad (8)$$

The element's vertical and rotational stiffness are governed by Eqs. (9)–(11), where the form and values for the numerical parameters are based on finite element simulations from Wolf [39] and Wolf and Song [40] for circular footings and Cremer et al. [8,9] for strip footings. Table 1 provides values for the uplift parameters to be consistent with the suggested values of Chatzigogos et al. [5]. The formulation was based on constant axial load, thus loadings involving large changes in axial load may not be accurately captured. For more information on the derivation of these equations see Chatzigogos et al. [6].

$$\kappa_{MN} = \kappa_{NN} \times \epsilon \left(1 - \frac{q_{m,uplift}}{q^{elastic}_m} \right) \qquad (9)$$

$$\kappa_{NM} = \kappa_{MN} \qquad (10)$$

$$\kappa_{MM} = \kappa_{MM} \gamma \delta \left(\frac{q_{m,uplift}}{q^{elastic}_m} \right)^{(\delta+1)} + \kappa_{NN} \epsilon^2 \left(1 - \frac{q_{m,uplift}}{q^{elastic}_m} \right)^2 \qquad (11)$$

2.3. Plasticity formulation

The plasticity formulation captures the non-linear response of the soil. The non-linear response is inelastic and therefore dissipates

energy, conceptually providing "hysteretic damping" to the soil-foundation-structure system, which is different to the energy loss through true viscous damping or radiation damping.

The plasticity formulation adopted in this model is based on the macro-element proposed by Figini et al. [15]. This formulation employs a rugby ball shaped bounding surface with a vertical mapping rule. A bounding surface approach allows for continuous plastic response, with the shape of the surface based on the experimentally determined ultimate loads surface from Nova and Montrasio [29] and almost identical to the experimentally determined surface of moment and axial load determined by Gajan et al. [16]. The rugby ball shape attempts to capture the reduction in the soil-footing contact area during uplift, which results in an increased load over the contact area and hence additional yield deformation. This is in contrast to the elliptic bounding surface centred at the origin as used in Chatzigogos et al. [6], which is based on a fully compliant footing and only the uplift model captures the reduction in compliant area.

The vertical mapping rule was justified by Figini et al. [15] due to most footings having loads paths mainly in the $Q_M − Q_V$ plane and therefore the projection to the bounding surface should follow the load increments. This assumption is certainly true for wall and bridge pier structures, however, frame structures can experience considerable variations in axial load as well, which may invalidate such an assumption. For further discussion on the use of a vertical mapping rule, please refer to Figini et al. [15].

The shape of the plasticity bounding surface is shown in Fig. 2 and is constructed through Eq. (12). The shape is governed through the parameters $Q_{V,max}$ and $Q_{M,max}$, which Figini et al. [15] suggest $Q_{V,max} = 3/4 \tan \phi$, ϕ being the soil friction angle and $Q_{M,max} = \Psi$. Ψ can be defined according to the ultimate capacity of the footing under eccentric loading, e.g. 0.48 from Vesic [38]. The other parameter, ξ, is often taken as 0.95 to follow the bounding surface formulation by Nova and Montrasio [29] with the advantage of having a vertical tangent at $Q_N = 1.0$, while a value of 1.0 for ξ would be in line with works by Georgiadis and Butterfield [18].

$$f_{BS}(Q) = \left(\frac{Q_V}{Q_{V,max}} \right)^2 + \left(\frac{Q_M}{Q_{M,max}} \right)^2 - Q_N^2 (1 - Q_N)^{2\xi} \qquad (12)$$

The macro-element model has a non-associated plastic flow rule defined by the plastic potential surface (G_{PS}). The shape of the plastic potential surface is expressed by Eq. (13) [15]. The shape takes the form of an ellipse centred on the origin in $Q_N − Q_V − Q_M$ space and the parameters λ and χ are introduced to control the radii.

$$G_{PS} = \lambda^2 \left(\frac{Q_V}{Q_{V,max}} \right)^2 + \chi^2 \left(\frac{Q_M}{Q_{M,max}} \right)^2 + Q_N^2 - 1 = 0 \qquad (13)$$

Values of $\lambda = 2.5$ and $\chi = 3.0$ were recommended by Figini et al. [14] as default values for predictive testing, however, these should be calibrated against experimental tests or finite element analysis results.

To compute the inverse plastic stiffness matrix (Γ^{-1}), the tensor product of the normal to the plastic potential surface and the bounding surface must be computed as in Eq. (14). In this equation n_g is the normal to the bounding surface and n is normal to the plastic potential surface at the vertically mapped image point (Fig. 3).

$$\Gamma^{-1} = \frac{1}{h} n_g \otimes n \qquad (14)$$

Table 1
Default values for strip and circular footings.

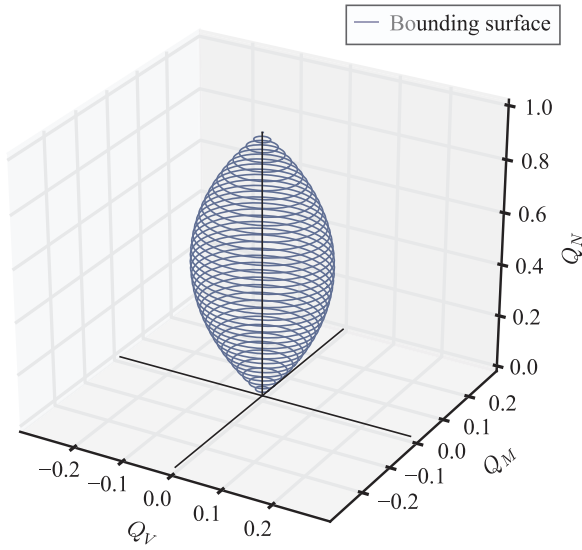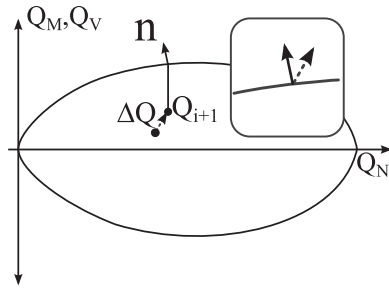|	α	ϵ	δ	γ
Strip	4.0	0.5	1.0	$1/\delta$
Circular	6.0	0.75	1.0	$1/\delta$

Fig. 2. Foundation bounding surface.

Fig. 3. Plasticity formulation with vertical mapping rule.

The parameter h defines the magnitude of plastic modulus and is determined through Eq. (15). The fitting parameter h_0 is a numerical constant in this formulation taken as some ratio (p_1) of κ_{NN} as in Eq. (16). The second parameter, Λ is the ratio of the distance to the vertically mapped image point on the bounding surface over the current load state (Q), taken from the Q_N axis as seen in Fig. 3 and given by Eq. (17).

$$h = h_0 \ln \Lambda \tag{15}$$

$$h_0 = p_1 \kappa_{NN} \tag{16}$$

$$\Lambda = \sqrt{\frac{Q_N^2 (1 - Q_N)^{2\xi}}{\left(\frac{Q_M}{Q_{M,max}}\right)^2 + \left(\frac{Q_V}{Q_{V,max}}\right)^2}} \tag{17}$$

To determine whether the element is loading (plastic response) or unloading/neutral loading (elastic only), the force increment (Q_{inc}) is projected onto n, a positive projection results in loading behaviour.

Soil has a less plastic response during reloading than during virgin loading. This increase in stiffness can be accounted for by replacing Eq. (15) with Eq. (18), where the parameter Λ_{min} is the lowest value of Λ obtained to this point in time during the loading history, and the parameter p_2 controls the increase in stiffness. For virgin loading $\Lambda = \Lambda_{min}$, which returns the same answer as Eq. (15). Figini et al. [15] suggests calibrating the parameter p_2 by fitting to the reloading stiffness of an experimental test but suggests $p_2 = 1.0$ for predictive testing.

$$h = h_0 \ln\left(\frac{\Lambda^{p_2+1}}{\Lambda_{min}^{p_2}}\right) \tag{18}$$

2.4. Coupling of uplift and plasticity

Based on work by Cremer et al. [8,9], the point of uplift initiation is affected by the level of soil non-linearity. Cremer suggests Eq. (19) to define the uplift moment, replacing Eq. (7) with:

$$Q_{M,0} = \pm \frac{Q_N}{\alpha} e^{-\zeta Q_N} \tag{19}$$

The parameter ζ varies based tendency for plastic deformation of the soil and Cremer et al. [8,9], suggests a value between 1.5 and 2.5.

2.5. Foundation radiation damping

Wave reflections at the soil-foundation interface result in large amounts of energy dissipating into the soil, which is referred to as geometric or radiation damping. It is essential to capture this energy loss in the numerical formulation, and for this purpose current set-up requires dashpot elements connected in parallel to the macro-element model in each degree-of-freedom.

2.6. Further numerical considerations

The proposed macro-element model has been implemented into the time history based structural analysis software Ruaumoko. To provide a numerically efficient and stable algorithm further modifications were required. The first being a state correction algorithm to ensure that the predicted level of force increment during a time step was inside the bounding surface creating a realistic loading state for the model. The second modification was to convert the non-symmetric stiffness matrix from the plasticity formulation into a symmetric form that could be used in the global stiffness matrix allowing for a more efficient matrix solving algorithm and global damping models to be used.

2.6.1. State correction algorithm

The state correction algorithm is used when a force increment causes a force state outside the bounding surface. This scenario is unrealistic and instead there should be a large reduction in stiffness associated with respectively large footing displacements without a large increase in forces. The state correction algorithm therefore takes the previous force state (which is inside the bounding surface) and scales back the force increment (by a 100th of the force increment) until it finds a force state that does not exceed the bounding surface (Fig. 4), the stiffness is then updated using the new force state. The new stiffness is very low because the force state is near failure and therefore the displacement increment does not result in a large force increment.

2.6.2. Dealing with a non-symmetric stiffness matrix

The non-associative behaviour in the plasticity formulation results in a non-symmetric tangent stiffness matrix. The non-symmetric stiffness matrix was converted into a symmetric form to be solved in the global stiffness matrix to determine the increment in displacement. The forces in the macro-element were then updated using the new displacement increments and the non-symmetric stiffness matrix. At this stage the forces may differ from those assumed in the end-of-step global equilibrium equation due to changes in stiffness as well as the error introduced due to the symmetric stiffness matrix. If the forces do not
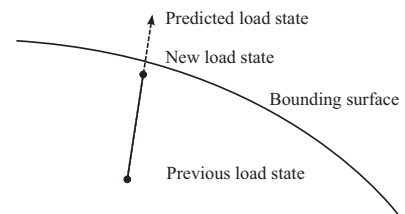

Fig. 4. New load state iterates until inside the bounding surface.

agree the error is used to adjust the incremental displacement so that full equilibrium is achieved. The symmetric matrix was formed by the average of the original matrix and its transpose (Eq. (20)).

$$K_{sym} = \frac{K_{nonsym} + K_{nonsym}^T}{2} \tag{20}$$

3. Simulation of seismic centrifuge tests

The proposed macro-element model was compared against two sets of centrifuge test data, where geometric and material properties were taken from the test reports and the uplift and plasticity formulations made use of the values suggested by Chatzigogos et al. [5] and Figini et al. [15]. The first set of experimental tests were of a pier structure on dry sand from the fifth experiment (LJD03) from the NEES project: "Innovative Economical Foundations with Improved Performance that is Less Sensitive to Site Conditions" [10]. The second set of experimental tests were of a one-bay, one-storey frame with isolated footings on dry sand from the first experiment (HBM02) from the NEES project: "Seismic performance assessments in dense urban environments" [23].

3.1. Pier structure experiments

3.1.1. Test set-up

The test set-up contained models of four bridge pier structures sitting on 183 mm (model scale) thick deposit of dry sand under enhanced gravity (49 g) using a centrifuge [10]. The single pier with a small footing shown in Fig. 5 (dimensions in prototype scale) was the primary interest for validation of the macro-element model .

The soil used in the tests was dry Nevada Sand with a relative density of 38% and internal angle of friction of 32° [10]. The soil shear modulus was determined based on the expression from Arulmoli et al. [1] using the void ratio and the effective confining stress from Perkins and Madson [33].

3.1.2. Pier ground motions

Table 2 summarises the ground motions used in the centrifuge tests, with the peak ground acceleration (PGA) and peak ground velocity (PGV) being the recorded values from free field surface accelerometers (average of GAH1 and GAH2 accelerometers (Fig. 7)). The goal of the experiments was to investigate the toppling behaviour of rocking foundations and therefore the motions had very high velocities. The bridge pier was subjected to 20 ground motions over four different centrifuge spins, however, the first eight motions were of very low amplitude and the data from these tests was not usable, as well as the data from motion ID5.

Fig. 6 shows the acceleration response spectra of the input ground motions for the numerical model.

3.1.3. Numerical model

The numerical simulation only modelled the behaviour in the plane of shaking and consisted of a lumped mass superstructure (M_{SS}) attached to a soil-foundation interface element (see Fig. 8 for geometric layout and input terms). The pier and deck were modelled linear-elastically as there were no reports of damage on the pier during testing. The superstructure damping was modelled with a rotational linear dashpot (C_{SS}) set to provide 5% of critical damping for relative lateral displacement between the foundation and the superstructure. The vertical displacement from the superstructure was slaved to the foundation node providing an axially perfectly rigid superstructure. The foundation mass (M_f) was modelled with horizontal and vertical masses.

The foundation radiation damping was modelled with vertical (C_{NN}), horizontal (C_{VV}) and rotational (C_{MM}), dashpots between the foundation and surrounding soil based on the radiation damping

equations from Gazetas [17]. All of the dashpots had a linear relationship between force and velocity, except for the vertical dashpot, which was limited to 1400 kN to avoid excessive damping forces that could make the macro-element unstable.

The initial stiffnesses (K_{NN}, K_{VV}, K_{MM}) for the macro soil-foundation element were determined from deter mined from Gazetas [17], where the correction for embedded foundations was not used as it was assumed that the contact area of the sidewalls was zero, as the numerical model was developed for shallow foundations on the surface. The foundation capacity (N_{cap}) was chosen to match that reported in Deng and Kutter [11] which was determined based on the shallow foundation bearing capacity equations from Salgado [35].

The pier stiffness (K_{SS}) was determined to match the reported natural frequency of the fixed base system of 0.84 Hz. Large displacement P-delta effects were considered in the analysis.

Table 3 summarises the input parameters used in the numerical model.

3.1.4. Comparison of results

The numerical prediction of the bridge pier response was compared against the measured experimental footing moment, footing rotation and footing settlement. Figs. 9 and 10 show the proposed model against the model from Chatzigogos et al. [5] and the experimental time series of the fourth and tenth motions respectively. The numerical model captured the general behaviour of the footing throughout the time series, and even gave reasonable estimates for the residual behaviour. The level of uplift as seen by the temporary upwards motion in the settlement plot was under estimated by the numerical model, however, there was good agreement with the timing of the peaks due to uplift and the general trend of the settlement.

The Chatzigogos et al. [5] model adopted the same values as those in Table 3 except that $Q_{V,max}$ and $Q_{M,max}$ were defined as the default values from Chatzigogos et al. [5] as 0.165 and 0.14 respectively. The Chatzigogos et al. [5] model provided reasonable estimates of moment, rotation and settlement, however, the modelled had much less plastic deformation at large rotations. The lower level of plasticity is reflected in the larger rotation values that were obtained in the later parts of the records, as the uplift dominants the rotational behaviour and therefore less energy is absorbed through plastic soil deformation. The Chatzigogos et al. [5] model also has much more plastic deformation at low rotations, this is seen in the large amount of foundation settlement under low oscillations at the end of both records. The plastic response of the Chatzigogos et al. [5] is almost constant throughout the whole motion since the ratio of current load to the maximum load using a radial mapping rule and bounding surface centred at the origin does not vary greatly under the applied moment and shear loading. The
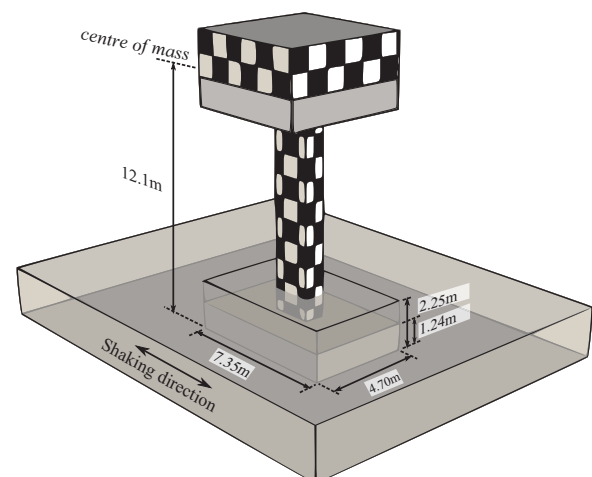

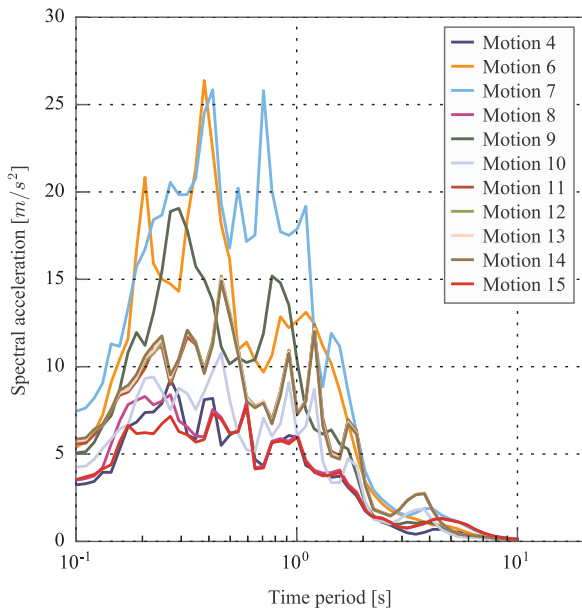**Fig. 5.** View of centrifuge model in prototype scale *after Deng and Kutter* [10].

Fig. 6. Pier input motions.

Fig. 8. Numerical model for bridge pier.

Table 2
Ground motions used in Pier test.

ID	Spin	PGA [g]	PGV [m/s]	Earthquake
4	2	0.31	0.34	1999 Chi-Chi earthquake (Filtered at 10 Hz)
6	3	0.53	0.76	1971 San Fernando earthquake
7	3	0.73	0.83	1976 Gazli earthquake
8	4	0.33	0.43	1999 Chi-Chi earthquake
9	4	0.49	0.54	1984 Morgan Hill earthquake
10	4	0.41	0.59	Four velocity pulses
11	4	0.53	0.76	Four velocity pulses
12	4	0.55	0.75	Four velocity pulses
13	4	0.54	0.74	Four velocity pulses
14	4	0.55	0.75	Four velocity pulses
15	4	0.33	0.39	1999 Chi-Chi earthquake

Table 3
Parameters used in pier numerical model.

Parameter	Value
Pier height	12.1 m
Superstructure mass (M_{SS})	553 T
Fixed base period (T_{SS})	1.2 s
Superstructure damping	5%
Footing length	7.35 m
Footing width	4.70 m
Footing depth	1.24 m
Footing embedment	2.24 m
Footing mass (M_f)	79 T
Soil initial shear modulus (G_{max})	23.5 MPa
Poisson's ratio (v)	0.3
Soil mass density (ρ)	1539 kg/m^3
Friction angle (ϕ)	32.7
Footing axial load capacity (N_{cap})	68.0 MN
Vertical stiffness (K_{NN})	603 MN/m
Horizontal stiffness (K_{VV})	447 MN/m
Rotational stiffness (K_{MM})	6330 MNm
Vertical radiation damping (C_{NN})	12.8 MNs/m
Horizontal radiation damping (C_{VV})	7.43 MNs/m
Rotational radiation damping (C_{MM})	18.9 MNms
Bounding surface shear parameter (μ)	0.469
Bounding surface moment parameter (ψ)	0.48
Bounding surface shape parameter (ξ)	0.95
Plasticity modulus factor (p_1)	0.2
Reload stiffness factor (p_2)	1.0
Plastic potential shear parameter (λ)	2.5
Plastic potential moment parameter (χ)	3.0

Fig. 7. Position of input ground motion sensors.

proposed model therefore captures the plastic response better than the Chatzigogos et al. [5] model because it is more sensitive to changes in the direction of the loading increment, and produces plastic flow that depends on both previous load state and current direction of loading increment (i.e. hypoplastic formulation). No comparison was made with the Figini et al. [15] due to the inherent limitations of the uplift model when implemented in finite element software, as discussed in Section 2.2.
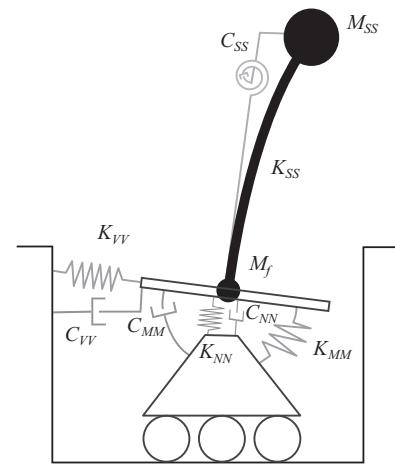
The peak foundation rotation obtained for all motions from the experiments and numerical predictions are compared in Fig. 11, with the percentage difference between the two values given in reference to the experimental value. The behaviour was generally very well predicted with most predictions being within 20% of the experimental values.

The modelling of the SFSI-induced settlement can be seen in Fig. 12, where the numerical predictions are compared against the experimental results. During the initial motions, the numerical model underestimated the level of settlement, possibly because the soil density was very low. However, the experimentally measured settlement reduced through subsequent tests. The input motions for motion 4 and 15 were nearly identical but the experimental settlement was 30 mm and 10 mm while the numerical model consistently predicted 17 mm. The behaviour is most clear when looking at the behaviour of the pulse type motions (motions 11–14), where the peak rotation is nearly identical for all
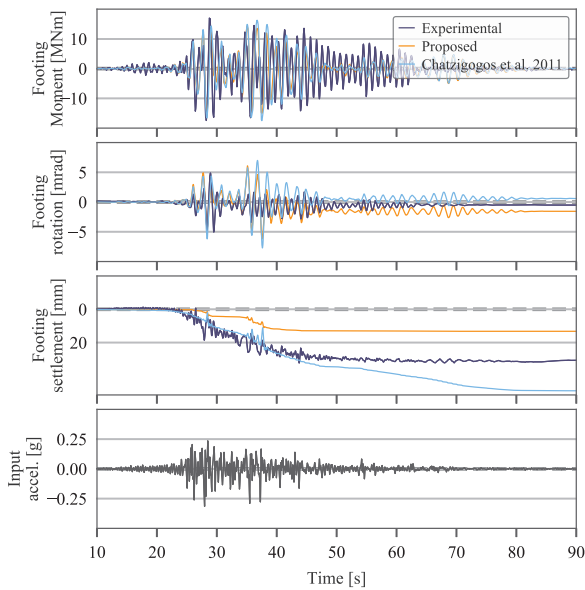
Fig. 9. Comparison of numerical and experimental behaviour of pier test - motion four.
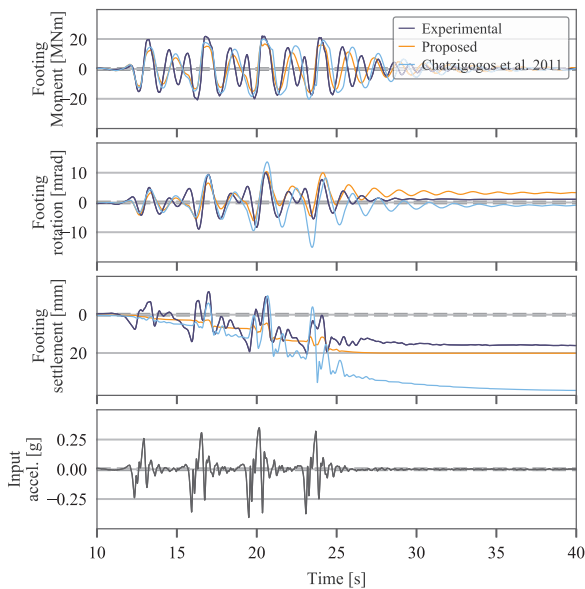

Fig. 10. Comparison of numerical and experimental behaviour of pier test - motion ten.
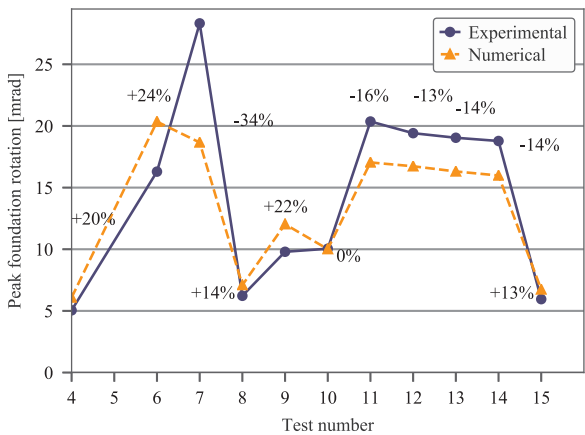

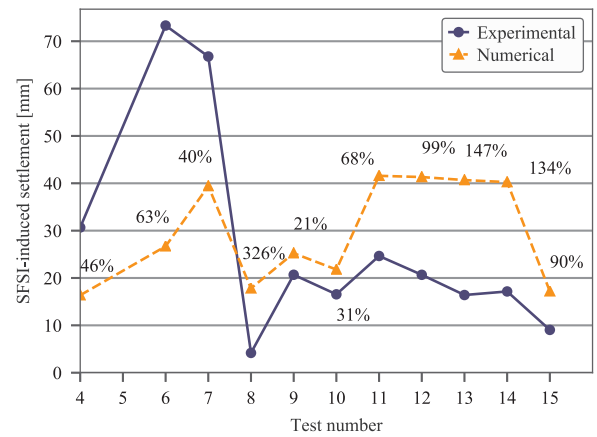**Fig. 11.** Comparison of peak rotation versus test number.

Fig. 12. Comparison of settlement versus test number.

motions (Fig. 11) and the numerical model predicts very similar settlements, however, the experiments show a decreasing trend in settlement. A possibly contributing factor to this trend was the densification of the soil, which started out at a relative density of 38% and the large amount of shaking caused 220 mm of free-field settlement (prototype scale), resulting in a relative density of 48%. Attempts were made to represent this by modifying the soil shear stiffness based a change in soil density due to the free-field settlement, but the modified shear stiffness made very little difference to the settlement and therefore was not shown here. This suggests that the mechanical properties of the soil directly under the foundation after long periods of shaking may be considerably different to the free-field, and this localised change caused a reduction in the tendency to settle.

It was seen in the time series plots that the trend of residual rotation was well predicted, however, the predicted final values were in some cases quite different to the experimental measurements. The comparison of the experimental and numerical residual rotations for all motions can be seen in Fig. 13.

The most notably poor estimate of residual rotation was test number six, where the residual rotation was in the opposite direction. The rotation time series is shown in Fig. 14, where it can be seen that the rotational behaviour is reasonably well captured except for at time = 38 s, where the footing rotates slightly more in the negative direction compared to the numerical model and subsequently results in residual deformation in the opposite direction. The high sensitivity of residual rotation to brief moments in the loading history makes it extremely difficult to model. However, in the assessment of structures for design it is less concerning, where the expected magnitude of residual deformation from a unknown hazard is more important than the exact value from an individual time history.
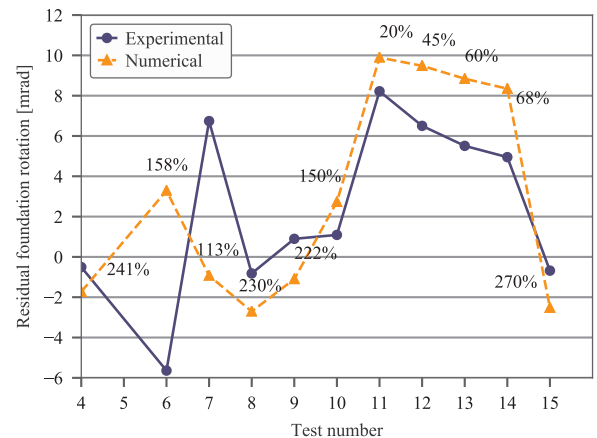

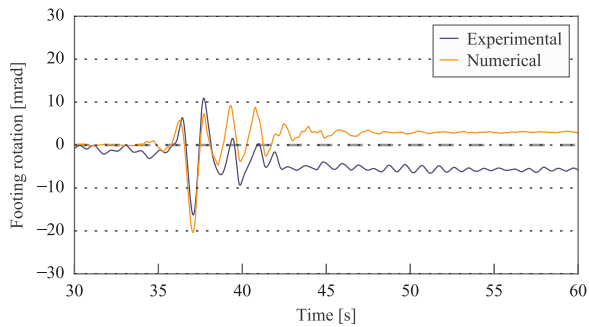**Fig. 13.** Comparison of residual rotation versus test number.

Fig. 14. Rotation time history of test six of pier structure.

3.2. One-bay frame experiments

3.2.1. Test set-up

The test set-up contained two model frame buildings sitting on 536 mm (model scale) of dry sand subject to enhanced gravitational conditions of 55 g using a centrifuge [23]. Fig. 15 shows the one-storey, one-bay frame building sitting on isolated footings, which was numerical modelled using the proposed macro-element model.

The soil used in the tests was dry Nevada Sand with a relative density of 80% and internal angle of friction of 40° according the test report [23]. The soil shear modulus ($G = 44\,MPa$) was taken from bender element tests conducted on a subsequent experiment (Test 3) at a depth of 4.4 m (prototype scale) [37].

3.2.2. Frame ground motions

The frame structure was subjected to 17 recorded ground motions over four centrifuge spins. The ground motions were applied in increasing levels of amplitude within each spin up and several ground motions were repeated between spin ups. Table 4 summarises the ground motions, with the peak ground acceleration (PGA) and peak ground velocity (PGV) being the recorded values from the accelerometers on the model ground surface. The input motion for the numerical model was taken as the measured surface acceleration from the free field accelerometer (HA14 accelerometer). For more information on the input motions please refer to page 67 in Trombetta [37]. The spin number refers to the centrifuge spin that the test was conducted on. Fig. 16 shows the acceleration response spectra of the field motions used as inputs into the numerical model.

3.2.3. Input parameters for the frame structure

The numerical model used in this study consisted of a two dimensional frame with lumped plasticity beam and columns elements attached to two soil-foundation macro-elements (Fig. 17). The roof mass (M_{SS}) was lumped at the beam centre and at the beam ends and the foundation masses (M_f) were lumped at the foundation level. The nonlinear behaviour in the hinges was assumed to be elasto-plastic in flexure and shear, with no flexure-shear-axial load interaction considered in the beams or column hinges. The column end blocks had some flexural stiffness to account for joint deformation which was taken as four times the stiffness of the full section flexibility.

The experimental frame hinges were deliberately reduced to provide localised plastic rotation. The cross-sections for the hinges are shown in Fig. 18, the beam type I cross-section was used for tests 1–12 and the beam type II cross-section was used for the remaining tests.

The moment-rotation relationships of the hinges were extracted from simple moment-rotation tests performed by the experimental team [41]. The mechanical and geometric properties of the sections are summarised in Table 5.

The foundation impedances were determined using the expressions from Gazetas [17]. Table 6 summarises the input parameters used for the frame numerical model. The two values listed for the mass and

period are for the first two centrifuge spins and the final two spins respectively, as the mass was reduced after the second spin.

3.2.4. Comparison of numerical and experimental results

The behaviour of the more complex frame structure was well predicted by the numerical model with Figs. 19 and 20 showing the time series behaviour for the LCN and WPI_H motions. The LCN motion was a low amplitude motion from the second spin up using the full mass and the type I beams. The WPI_H motion was a high amplitude motion from the last spin up using the reduced mass and the type II beams.

The time series roof displacement was well captured by the numerical model for the LCN motion and had generally lower amplitude in WPI_H motion. The footing rotation behaviour was fairly consistent for the right footing, however, the left footing contained an additional high frequency component that was not observed in the numerical model results. The numerical model captured the majority of the footing vertical motion for the LCN motion and provided an excellent estimate of the settlement, however, the model was less consistent in the stronger WPI_H motion. A similar level of accuracy was obtained for all centrifuge tests.

The comparison of peak foundation rotation for all tests between the experimental and numerical values can be seen in Fig. 21, with the percentage difference between the two values given in reference to the experimental value. All motions except for the motions in sequence one and the last motion WVC_H are shown, as in these motions the high frequency content of the footing was not recorded.

The behaviour was generally well predicted, although not as well as the foundation peak rotation for the pier. The comparative difference between the numerical and experimental values was fairly consistent through the entire set of tests with the worst difference in absolute terms occurring during the strong SCS_H motion.

The SFSI-settlement can be assessed for all motions for both the experimental and numerical results in Fig. 22. The numerical settlement was reasonably consistent with the experimental values and just like in the pier test, the settlement was under-estimated in the earlier tests and over-estimated in the later tests. The magnitude of the settlement was similar to the level observed in the pier tests with largest being 91 mm and the average being 15 mm from all of the motions. As expected the larger settlement values (motions SCS_H, JOS_H and PRI) all correspond to large peak rotation values as seen in Fig. 21.

In Fig. 23 the numerical residual rotation can be compared to the experimental values for all of the ground motions. The numerical model did not capture the residual rotation of the experiment very well. The signed residual rotation is shown to demonstrate that the numerical model sometimes predicted a residual rotation in the opposite direction to the experimentally measured value. The residual rotation is more difficult to capture as it is more dependant on the plastic response of a single cycle, while the settlement is a cumulative measure of plastic
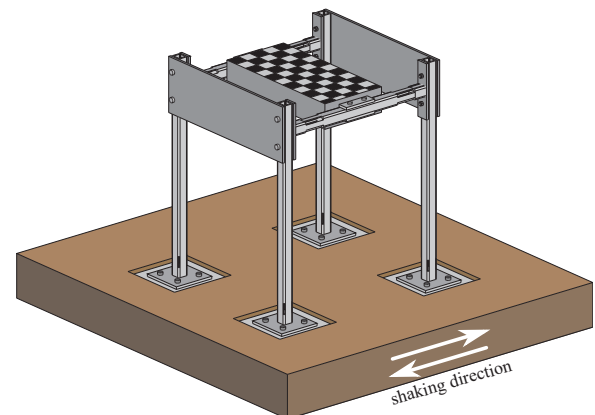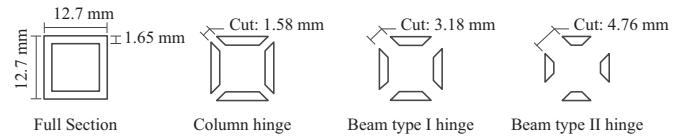

Fig. 15. Test setup *after* Mason et al. [23].

Table 4
Ground motions used in Frame test.

ID	Spin	PGA (g)	PGV (m/s)	Earthquake
JOS_L_1	1	0.14	0.16	1992 Landers
TCU_L	1	0.23	0.21	1999 Chi Chi
RRS	1	0.38	0.52	1994 Northridge
PTS	2	0.19	0.25	1987 Sup. Hills
SCS_L_1	2	0.31	0.32	1994 Northridge
LCN	2	0.34	0.52	1992 Landers
JOS_L_2	3	0.17	0.16	1992 Landers
SCS_L_2	3	0.32	0.32	1994 Northridge
WVC_L	3	0.40	0.51	1989 Loma Prieta
SCS_H	3	0.61	0.77	1994 Northridge
JOS_H	3	0.47	0.49	1992 Landers
WPI_L	3	0.39	0.56	1994 Northridge
JOS_L_3	4	0.16	0.16	1992 Landers
WPI_H	4	0.46	0.66	1994 Northridge
PRI	4	0.71	0.75	1995 Kobe
TCU_H	4	0.46	0.35	1989 Chi Chi
WVC_H	4	0.44	0.68	1989 Loma Prieta

Fig. 16. Frame input motions.
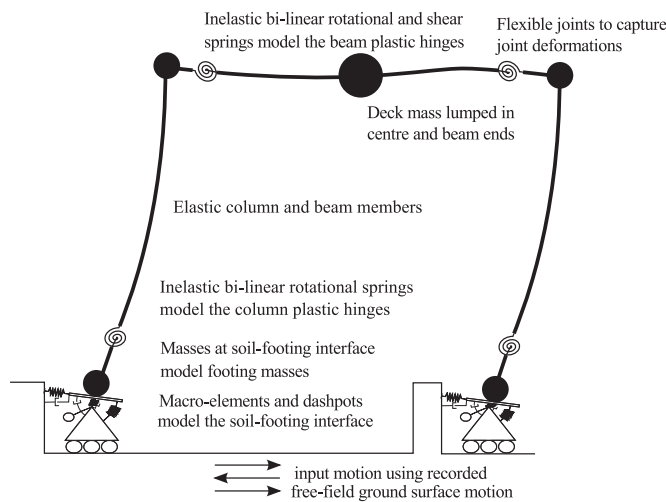
Fig. 17. Numerical models of soil and structure system.

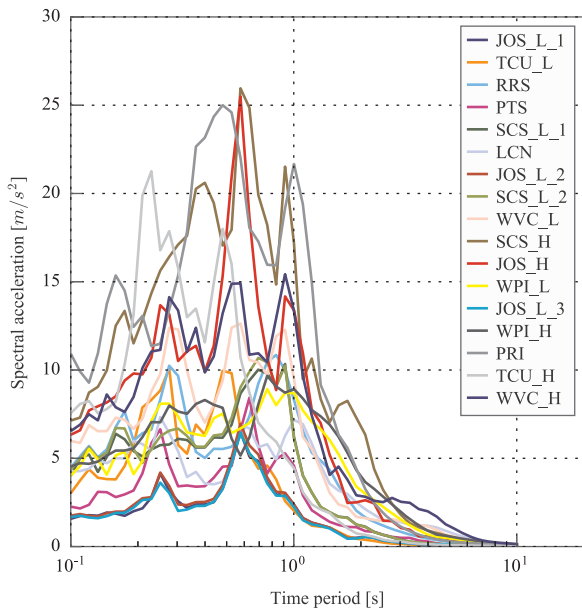**Fig. 18.** Model scale member cross-sections.

Table 5
Parameters used in numerical model.

Member	Column	Beam I	Beam II	Full
Initial rotational stiffness [MNm^2]	750	617	783	2780
Yield moment [MNm]	10.0	5.0	8.2	–
Post yield rotational stiffness ratio	0.16	0.09	0.06	–
Yield shear force [MN]	17.5	3.5	9.7	–
Hinge length [m]	0.72	1.4	0.7	–

Table 6
Parameters used in frame numerical model.

Parameter	Value
Column height	12.8 m
Beam length	9.96 m
Superstructure mass (M_{SS})	443 T, 368 T (per frame)
Fixed base period (T_{SS})	1.0 s, 0.88 s
Superstructure damping	2%
Non-linear superstructure	see Section 3.2.3
Footing length	4.37 m
Footing width	4.37 m
Footing depth	0.87 m
Footing embedment	1.16 m
Footing mass (M_f)	522 T
Soil initial shear modulus (G_{max})	44 MPa
Poisson's ratio (v)	0.3
Soil mass density (ρ)	1700 kg/m^3
Friction angle (ϕ)	40.0
Footing axial load capacity (N_{cap})	58.0MN
Vertical stiffness (K_{NN})	617 MN/m
Horizontal stiffness (K_{VV})	504 MN/m
Rotational stiffness (K_{MM})	2414 MNm
Vertical radiation damping (C_{NN})	8.03 MNs/m
Horizontal radiation damping (C_{VV})	5.20 MNs/m
Rotational radiation damping (C_{MM})	4.47 MNms
Bounding surface shear parameter (μ)	0.565
Bounding surface moment parameter (ψ)	0.48
Bounding surface shape parameter (ξ)	0.95
Plasticity modulus factor (p_1)	0.2
Reload stiffness factor (p_2)	1.0
Plastic potential shear parameter (λ)	2.5
Plastic potential moment parameter (χ)	3.0

response. Further issues with the prediction of residual deformations arose due to the dissipation of the static footing moment that occurred in each of the numerical model simulations that may not have occurred for each experimental test due to the tests being run in a sequence. This dissipation of moment was accompanied by a permanent rotation of the footing.

3.3. Discussion on experimental validation

The examination of the time series of several simulations showed that the transient behaviour throughout the excitation was well modelled. The majority of the simulations from both tests predicted peak foundation rotations, SFSI-induced settlement and residual rotation values within 30%, 10 mm, 80% respectively. The numerical model tended to under-predict the SFSI-induced settlement and residual
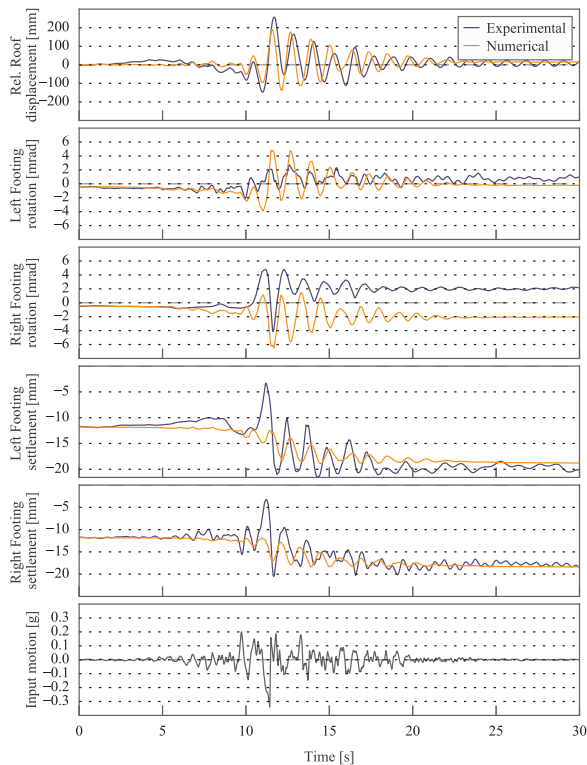
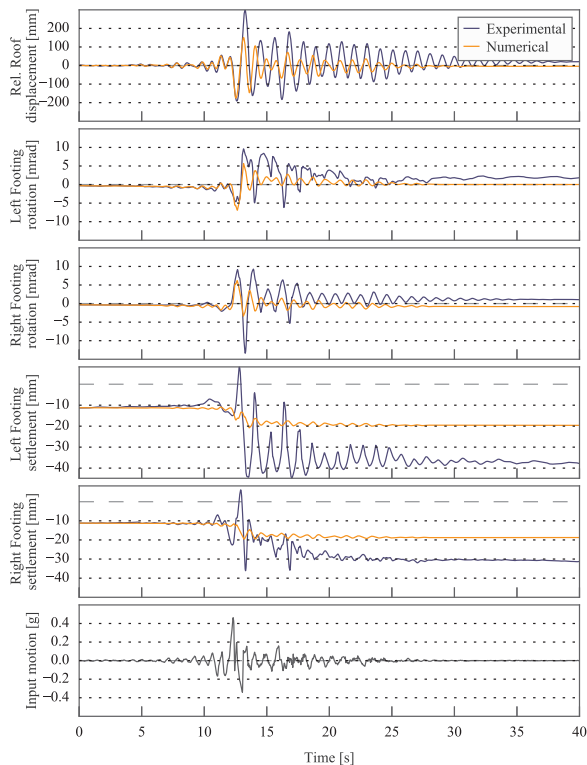**Fig. 19.** Comparison of numerical and experimental behaviour of footings and structure in frame test - motion LCN.

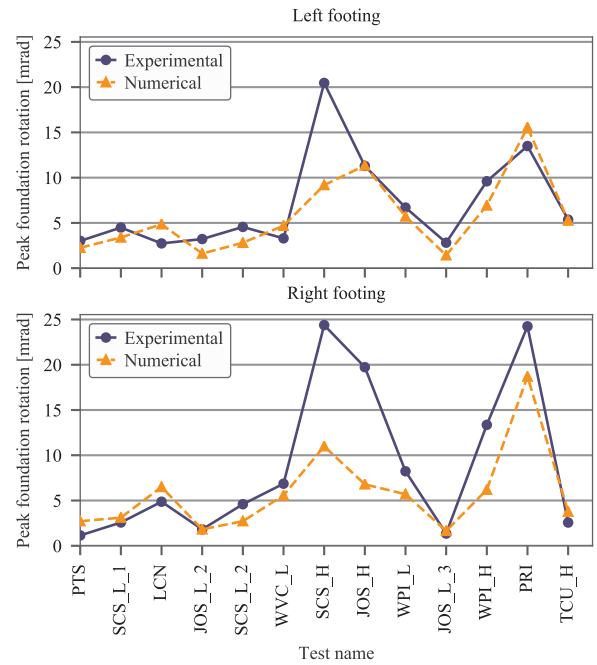**Fig. 20.** Comparison of numerical and experimental behaviour of footings and structure in frame test - motion WPI_H.

Fig. 21. Comparison of peak foundation rotation - all motions.
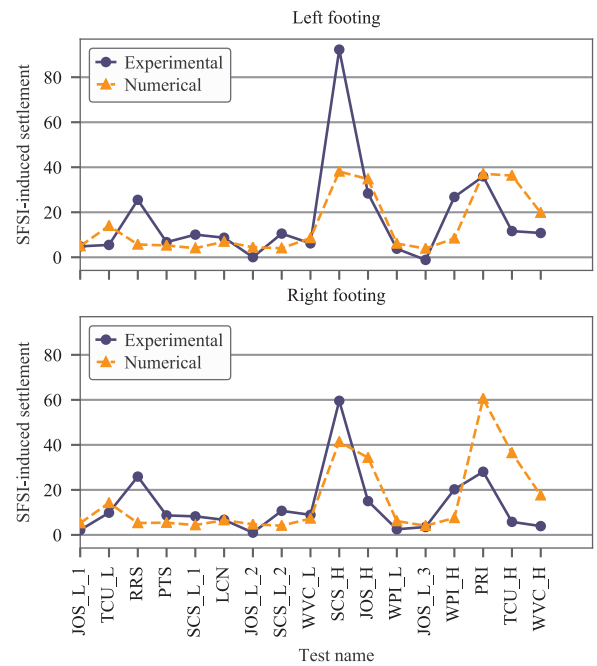
Fig. 22. Comparison of rotation-settlement behaviour - all motions.

deformation in the earlier motions and over-predicted them in later motions, suggesting that the behaviour of the experimental model was modified due to local densification of the soil beneath the footings.

Most importantly, all of the input values for the macro-element used

values suggested in literature, the physical and geometric properties of the numerical model were all taken from the test reports and the input ground motions were the recorded free field motions, thus the presented results can be assessed as class C predictions.

4. Limitations and future opportunities

There are several limitations to the proposed macro-element formulation that should be understood before making use of it. The model uses a vertical mapping rule and therefore cannot predict plastic behaviour under purely axial loading. This is not an issue for piers and non-coupled walls as there is very little variation in axial load, however, it can be an issue for the outer columns of moment resisting
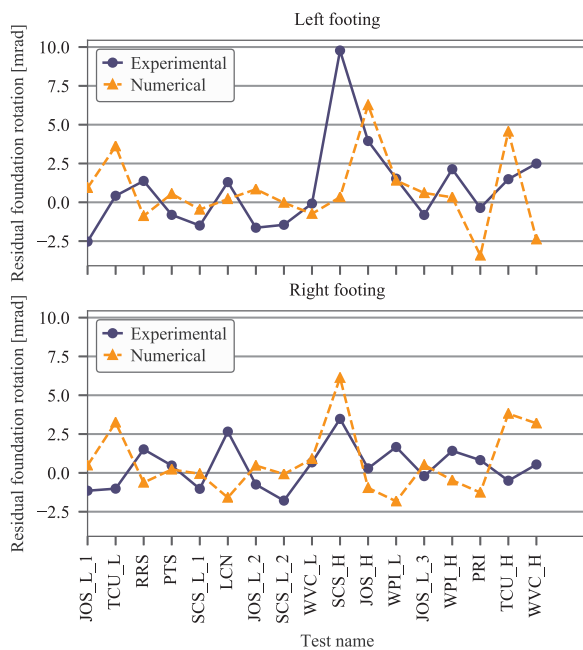
Fig. 23. Comparison of computed peak rotation and residual rotation with respective measured values for all motions.

frames or coupled walls where the dynamic variation in axial load from frame action is significant. In the frame test the vertical load only varied by 15–25%, and therefore inconsistent behaviour could still be expected under more extreme variations in axial load.

The use of an ellipsoidal shape provides a convenient mathematical expression for the bounding surface and plastic potential surface; however research by Gourvenec [20] has shown dependence on whether the moment and shear are acting in the same direction which would result in a skewed ellipsoidal shape. This is due to the increased shear stress when loads are in the same direction, however, the magnitude of the effect does not warrant the additional complexity. The slightly different bounding surfaces that are obtained for different shaped footings based on work by Gottardi and Houlsby [19], Gourvenec [20] and Bransby and Randolph [3] are also not accounted for.

For modelling radiation damping in the soil, the current formulation uses dashpot elements that are connected in parallel to the macro-element. This affects the uplift and plasticity models as they should be based on the applied forces, but instead use the applied forces minus the dashpot forces. The difference is only significant during large uplift and could be accounted for by including the viscous energy dissipation into the macro-element formulation. However, the development of a viscous macro-element is not trivial given that the uplift and plasticity models are based on static behaviour and therefore the modification to soil properties during dynamic loading should also be accounted for.

The large damping forces that can be generated during uplift may not be realistic either as during uplift the footing is not releasing large amounts of energy into the ground; however, this is somewhat balanced by the impact loading when the footing returns to the surface which can dissipate considerable energy. A modification to the vertical dashpot element to limit the damping force to 20% of the applied axial load provides a simple approximation to the complex dynamic behaviour and energy dissipation during footing uplift.

The current macro-element model only accounts for soil stiffness degradation through shear induced by the structure, however, the soil under the structure undergoes additional shear deformation and potentially a reduction in stiffness due to ground shaking.

5. Conclusions

This paper presents a macro-element formulation for predictive assessment of the effects of SFSI. The model captures the major non-linear aspects of SFSI through two interacting constitutive models. The plasticity model captures the effects of soil yielding, while the uplift model captures the geometric non-linearities during footing uplift.

The macro-element was implemented in the time history analysis software Ruaumoko3D and numerical simulations were compared to two sets of seismic centrifuge tests. In the first experiment, a pier structure was shaken to levels close to toppling using both recorded and pulse type ground motions. The second experiment was a one bay, single storey frame structure with a non-linear superstructure and isolated footings, exposed to recorded ground motions at varying levels of intensity.

In both cases the macro-element model provided suitable simulation of the transient behaviour of the foundation and superstructure. The model also provided reasonable estimates of settlement and in some cases the residual foundation rotation was also modelled accurately. The macro-element provides an intuitive and numerical efficient tool for simulating complex non-linear soil-foundation-structure interaction.

The validation and continued development of soil-foundation macro-elements is a promising path forward to allow SFSI to be widely considered and understood in structural engineering. The development and implementation of this macro-element was a key step towards the development of integrated displacement-based design and assessment procedure for building-foundation systems [24,25].

References

[1] Arulmoli K, Muraleetharan KK, Hosain MM, Fruth LS. VELACS laboratory testing program, soil data report. Technical report, Irvine, CA; 1992.
[2] Bienen B, Byrne BW, Houlsby GT, Cassidy MJ. Investigating six-degree-of-freedom loading of shallow foundations on sand. Géotechnique 2006;57(5):483–4.
[3] Bransby MF, Randolph MF. Combined loading of skirted foundations. Géotechnique 1998;48(5):637–55.
[4] Carr AJ. Ruaumoko, Non-linear Time-history Analysis Program. University of Canterbury, New Zealand. Carr Research Ltd, Christchurch, New Zealand; 2015.
[5] Chatzigogos CT, Figini R, Pecker A, Salençon J. A macroelement formulation for shallow foundations on cohesive and frictional soils. Int J Numer Anal Methods Geomech 2011;35(8):902–31.
[6] Chatzigogos CT, Pecker A, Salençon J. Macroelement modeling of shallow foundations. Soil Dyn Earthq Eng 2009;29:765–81.
[7] Combescure D, Chaudat T. ICONS European program seismic tests on R/C walls with uplift CAMUS 4 specimen. Technical report; 2000.
[8] Cremer C, Pecker A, Davenne L. Cyclic macro-element for soil-structure interaction: material and geometrical non-linearities. Int J Numer Anal Methods Geomech 2001;25(13):1257–84.
[9] Cremer C, Pecker A, Davenne L. Modelling of nonlinear dynamic behaviour of a

shallow strip foundation with macro-element. J Earthq Eng 2002:175–211.

[10] Deng L, Kutter BL. Seismic performance of bridge systems with rocking foundations: centrifuge data report for LJD03. Technical report; 2010.

[11] Deng L, Kutter BL. Characterization of rocking shallow foundations using centrifuge model tests. Earthq Eng Struct Dyn 2012;41(5):1043–60.

[12] di Prisco C, Nova R, Sibilia A. Shallow Footings Under Cyclic Loading: Experimental Behaviour and Constitutive Modeling. Geotechnical Analysis of Seismic Vulnerability of Historical Monuments; 2003.

[13] El Ganainy H, El Naggar MH. Efficient 3D nonlinear Winkler model for shallow foundations. Soil Dyn Earthq Eng 2009;29(8):1236–48.

[14] Figini R. Non-linear dynamic soil-structure interaction: Application to seismic analysis and design of structures on shallow foundations. Ph.D. Thesis, Politecnico di Milano; 2010.

[15] Figini R, Paolucci R, Chatzigogos CT. A macro-element model for non-linear soil-shallow foundation-structure interaction under seismic loads: theoretical development and experimental validation on large scale tests. Earthq Eng Struct Dyn 2012;41(3):475–93.

[16] Gajan S, Kutter BL, Phalen JD, Hutchinson TC, Martin GR. Centrifuge modeling of load-deformation behavior of rocking shallow foundations. Soil Dyn Earthq Eng 2005;25(7–10):773–83.

[17] Gazetas G. Foundation Vibrations. In: Foundation Engineering Handbook; 1991. p. 553–93.

[18] Georgiadis M, Butterfield R. Displacement of footings on sand under eccentric and inclined loads. Can Geotech J 1988:199–212.

[19] Gottardi G, Houlsby G. Plastic response of circular footings on sand under general planar loading. Geotechnique 1999;49(4):453–69.

[20] Gourvenec S. Shape effects on the capacity of rectangular footings under general loading. Géotechnique 2007;57(8):637–46.

[21] Harden CW, Hutchinson TC. Beam-on-Nonlinear-Winkler-Foundation Modeling of Shallow, Rocking-Dominated Footings. Earthq Spectra 2009;25(2):277–300.

[22] Houlsby G, Martin C. Jackup units on clay: structural analysis with realistic modelling of spudcan behaviour. Predictive Soil Mechanics; 1993.

[23] Mason HB, Trombetta NW, Gille NW, Lund JN, Zupan JD, Puangnak H, et al. Seismic performance assessment in dense urban environments: Centrifuge data report for HBM02. Technical Report August; 2010.

[24] Millen MDL, Integrated Performance based of building-foundation systems, Ph.D. Thesis, University of Canterbury; 2015. https://ir.canterbury.ac.nz/handle/10092/12138 Spectra; 2017 (submitted for publication).

[25] Millen MDL, Pampanin S, Cubrinovski M. Displacement-based design of soil-foundation-structure systems. Proceedings of ICE Geotech Eng; 2018 (submitted for publication). Dynamics, submitted 2017b.

[26] Moghaddasi M, Carr AJ, Pampanin S, Chase JG, Pecker A. The effects of soil-foundation interface nonlinearity on seismic soil-structure interaction analysis. In 2012 NZSEE Conference, 2012; p. 1–14.

[27] Mylonakis G, Nikolaou S, Gazetas G. Footings under seismic loading: analysis and design issues with emphasis on bridge foundations. Soil Dyn Earthq Eng 2006;26(9):824–53.

[28] Negro P, Paolucci R, Pedretti S, Faccioli E. Large scale Soil-structure Interaction Experiments on sand under cyclic loading. Proceedings of the Twelfth World Conference of Earthquake Engineering; 1999. p. 1–8.

[29] Nova R, Montrasio L. Settlements of shallow foundations on sand. Géotechnique 1991;41(2):243–56.

[30] Paolucci R. Simplified evaluation of earthquake-induced permanent displacements of shallow foundations. J Earthq Eng 1997;1(3):563–79.

[31] Paolucci R, Shirato M, Yilmaz MT. Seismic behaviour of shallow foundations: shaking table experiments vs numerical modelling. Earthq Eng Struct Dyn 2008;37(4):577–95.

[32] Pecker A, Chatzigogos CT. Non linear soil structure interaction: impact on the seismic response of structures. In: IX European Conference on Earthquake Engineering, Ohrid, FYROM; 2010. p. 1–26.

[33] Perkins SW, Madson CR. Bearing capacity of shallow foundations on sand: a relative density approach. J Geotech Geoenviron Eng 2000;126(6):521–30.

[34] Roscoe KH, Schofield. The stability of short pier foundations on sand. British Welding Journal; 1957.

[35] Salgado R. The engineering of foundations. New York: McGraw Hill; 2008.

[36] Shirato M, Kouno T, Asai R, Nakatani S, Fukui J, Paolucci R. Large-scale experiments on nonlinear behavior of shallow foundations subjected to strong earthquakes. Soils Found 2008;48(5):673–92.

[37] Trombetta NW. Seismic Soil-Foundation-Structure Interaction in Urban Environments. Ph.D. Thesis, San Diego; 2013.

[38] Vesic AS. Bearing capacity of shallow foundations. In: Winterkorn HF, Fang HY, editors. Foundations engineering handbook. 1975. p. 121–47.

[39] Wolf JP. Soil-structure interaction analysis in the time domain. New Jersey: Prentice Hall; 1988.

[40] Wolf JP, Song C. Some cornerstones of dynamic soil-structure interaction. Eng Struct 2002;24(1):13–28.

[41] Mason HB, 2014, Personal communication.